

Automated cross-sectional view selection in CT angiography of aortic dissections with uncertainty awareness and retrospective clinical annotations

Antonio Pepe^{a,b,c,*}, Jan Egger^{c,d,*}, Marina Codari^b, Martin J. Willemink^b, Christina Gsaxner^{a,c}, Jianning Li^{c,d}, Peter M. Roth^a, Gabriel Mistelbauer^{b,e}, Dieter Schmalstieg^a, Dominik Fleischmann^b

^aGraz University of Technology, Institute of Computer Graphics and Vision, Inffeldgasse 16/II, 8010 Graz, Austria.

^bStanford University, School of Medicine, 3D and Quantitative Imaging Lab, 300 Pasteur Drive Stanford, CA 94305, USA.

^cComputer Algorithms for Médecine (Café) Laboratory, Graz, Austria.

^dUniversity Medicine Essen, Institute for AI in Medicine (IKIM), Girardetstraße 2, 45131 Essen, Germany.

^eOtto-von-Guericke University. Department of Simulation and Graphics. Universitätsplatz 2, 39106 Magdeburg, Germany.

Abstract

Objective: Surveillance imaging of chronic aortic diseases, such as dissections, relies on obtaining and comparing cross-sectional diameter measurements at predefined aortic landmarks, over time. Due to a lack of robust tools, the orientation of the cross-sectional planes is defined manually by highly trained operators. We show how manual annotations routinely collected in a clinic can be efficiently used to ease this task, despite the presence of a non-negligible interoperator variability in the measurements. *Impact:* Ill-posed but repetitive imaging tasks can be eased or automated by leveraging imperfect, retrospective clinical annotations. *Methodology:* In this work, we combine convolutional neural networks and uncertainty quantification methods to predict the orientation of such cross-sectional planes. We use clinical data randomly processed by 11 operators for training, and test on a smaller set processed by 3 independent operators to assess interoperator variability. *Results:* Our analysis shows that manual selection of cross-sectional planes is characterized by 95% limits of agreement (LOA) of 10.6° and 21.4° per angle. Our method showed to decrease static error by 3.57° (40.2%) and 4.11° (32.8%) against state of the art and LOA by 5.4° (49.0%) and 16.0° (74.6%) against manual processing. *Conclusion:* This suggests that pre-existing annotations can be an inexpensive resource in clinics to ease ill-posed and repetitive tasks like cross-section extraction for surveillance of aortic dissections.

Keywords: imperfect annotations, aortic dissection, measurement, reproducibility, double-oblique reformation

*Corresponding authors and shared first authorship.

Email addresses: apepe@stanford.edu (Antonio Pepe), jan.egger@uk-essen.de (Jan Egger), mcodari@stanford.edu (Marina Codari), willemink@stanford.edu (Martin J. Willemink), gsaxner@tugraz.at (Christina Gsaxner), jianning.li@uk-essen.de (Jianning Li), pmroth@icg.tugraz.at (Peter M. Roth), gmistelbauer@isg.cs.uni-magdeburg.de (Gabriel Mistelbauer), schmalstieg@tugraz.at (Dieter Schmalstieg), d.fleischmann@stanford.edu (Dominik Fleischmann)

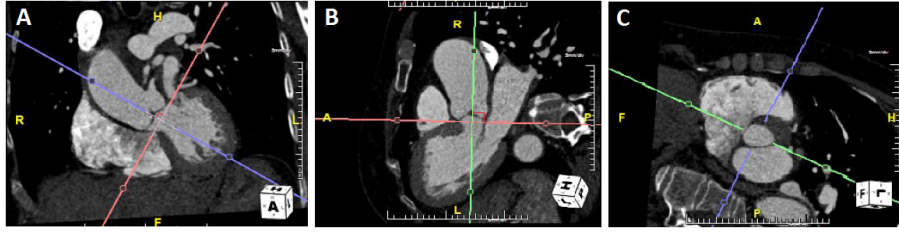


Figure 1: Example of a double-oblique reformation applied to extract the cross-sectional view of an aortic annulus. The red planes (left and central images) are adjusted so that they are locally orthogonal to the aorta from two different orientations. The violet and green planes are parallel to the local blood flow direction. For the specific location, the orthogonal cross section is described by the red plane (rightmost figure).

1. Introduction

Cross-sectional views are regularly used for the analysis of vascular structures in computed tomography angiography (CTA) images (Müller-Eschner et al. (2013); Rajiah (2013); Erbel et al. (2014); Gamechi et al. (2019)). Patients with chronic aortic diseases, such as aneurysms and dissections, require life-long surveillance and serial imaging to detect aneurysm growth and prevent fatal aortic rupture (Lau et al. (2017)). The most important information sought in aortic surveillance imaging is aortic caliber. An accurate determination of aortic caliber requires that diameter measurements are obtained on cross-sections oriented orthogonal to the aortic flow channel (Erbel et al. (2014); Lombardi et al. (2020); Pepe et al. (2020)). In clinical practice, the selection and orientation of these cross-sectional views, or planes, is defined manually by highly trained radiologists and radiology technicians, using free-hand interactive double-oblique reformations (Díaz-Peláez et al. (2017); Bhave et al. (2018)) or semi-automatic techniques that track the vessel centerline (Müller-Eschner et al. (2013); Gamechi et al. (2019)). Figure 1 and Figure 2 provide examples of these methodologies.

The manual, free-hand estimation of these cross-sectional views and measurements is not only time-consuming, requiring about 15 minutes per patient, but the resulting measurements are also operator-dependent: Nienaber et al. (2016) showed that the interoperator and intraoperator variabilities for cross-sectional diameter measurements in CTA images of aortic aneurysms and dissections are ± 5 mm and ± 3 mm, respectively. This introduces a considerable uncertainty in clinical decision making, where indications for surgical repair are based on a measurement threshold of 55 mm (Heuts et al. (2020)). The centerline-based approaches have been validated in patients with patent and unaltered flow channels (Gamechi et al. (2019)). However, just the presence of eccentric thrombus within an aneurysm introduces significant inaccuracies in centerline-based diameter measurements (Egger et al. (2012); Krissian et al. (2014); Kaufhold et al. (2018)). The morphologic changes related to aortic dissection (AD), where a second blood-flow channel forms between the layers of the aortic wall, often prohibit the use of automated centerline extraction methods (Pepe et al. (2020)). Figure 3 and Figure 4 show the differences between a healthy aortic lumen and a case

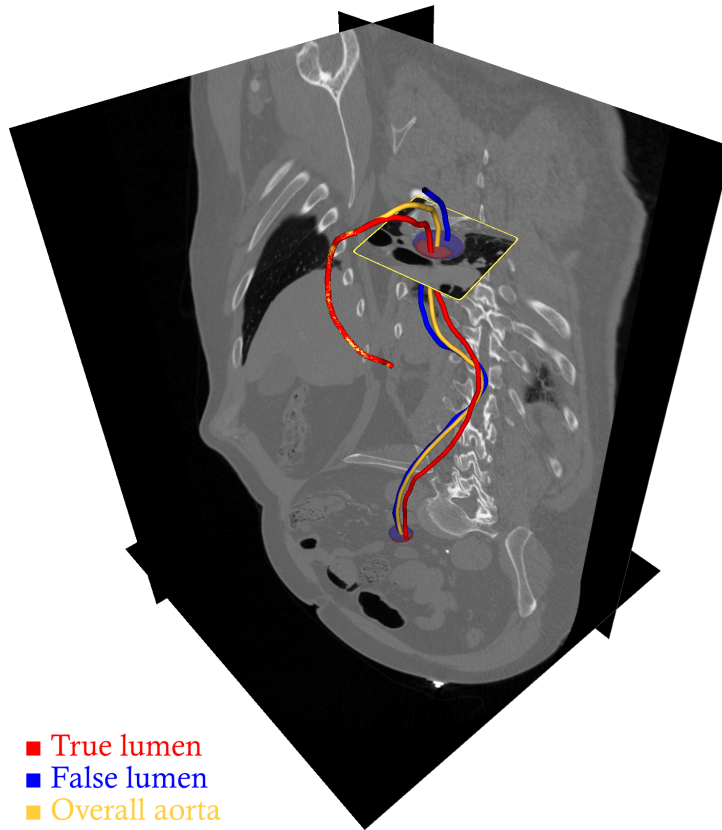


Figure 2: Examples of centerlines obtained through tinning of segmentation. The yellow line represents the centerline of the overall aorta. The direction of this centerline is used for surveillance purposes. The red and blue lines represent the true and false lumina, respectively. In this example, the false lumen originates in the descending aorta. It can be seen how the overall direction of the aorta is not necessarily matching the direction of each single lumen.

of AD, where also a second flow channel (false lumen) is present. The flow channels are typically asymmetric, often with different contrast medium opacification (i.e. voxel intensity), tortuous and twisting around each other (Figure 4, right), and both – the original true lumen and the new, so-called false lumen of the dissected aorta – can contain thrombus. Thus, in patients with aortic dissection, the time consuming and operator-dependent manual selection is standard of care. The existence of clinical-grade labels – while recognizing and accounting for their known limitations – provide an opportunity to pursue an alternative approach, improving the speed and reproducibility of aortic measurements (Houben et al. (2020)).

Contribution. In this work, we show how an uncertainty-aware convolutional neural network (CNN) can be trained on imperfect annotations obtained in a routine clinical setting, to extract cross-sections with higher reproducibility, and within the accuracy

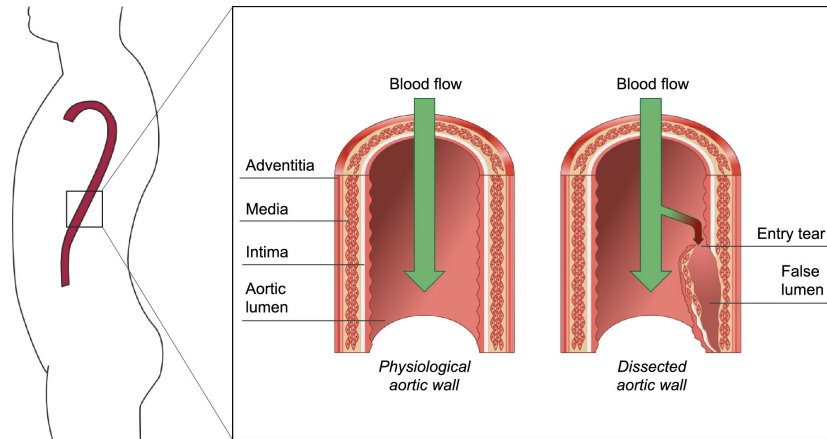


Figure 3: Computer-generated visualization of the aortic wall, of its different layers, and of its deformation due to the formation of an entry tear (Pepe et al. (2020)).

of current clinical practice standards. In particular, we:

- provide an overview of the clinical needs and the potential of data-driven methods, such as deep learning (section 2),
- formulate our research hypothesis and propose an uncertainty-aware deep learning method for the automation of the clinical work based on existing clinical annotations (section 3),
- compare the proposed method with other state-of-the-art algorithms and with the interoperator variability of three independent experts (section 4), and
- discuss the role and impact of uncertainty quantification for the utilization of raw clinical annotations from different experts (section 5).

To the best of our knowledge, this is the first investigation of uncertainty-aware deep learning approaches for the extraction of cross-sectional views in CTA images with a chronic aortic disease, for which the common tubular prior does not hold.

2. Background

In this section, we provide a general overview of the pathology (subsection 2.1) and the current clinical surveillance protocols (subsection 2.2). Readers with a strong cardiovascular background might want to skip this initial overview. Afterwards, we analyze current state-of-the-art algorithms for the image processing (subsection 2.3) and discuss the impact that uncertainty-aware deep learning algorithms can have (subsection 2.4).

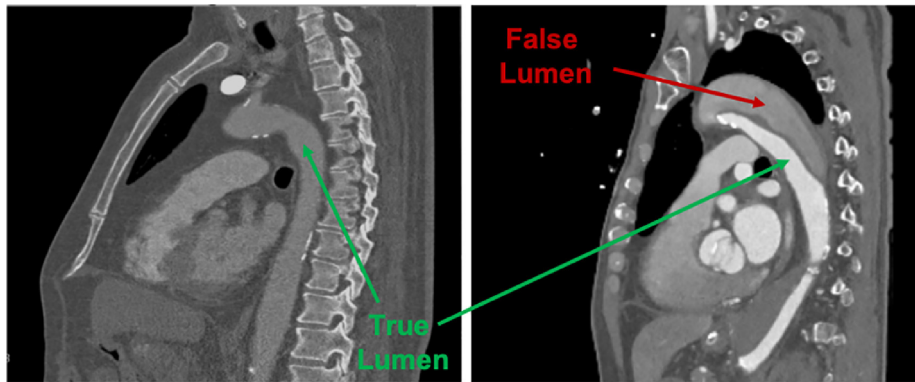


Figure 4: Computed tomography angiography of a healthy subject (left), where only one lumen is visible in the aorta; an aortic dissection case (right), where the false and true lumina are clearly distinguishable (Pepe et al. (2020)).

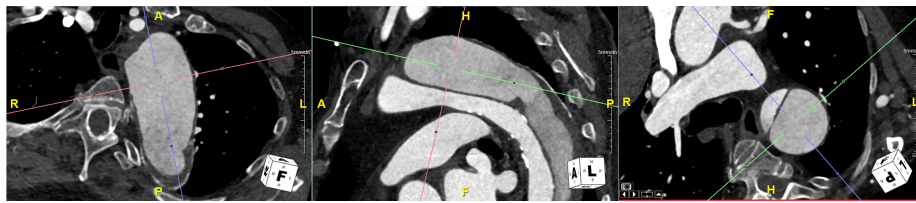


Figure 5: Example of a double-oblique reformation applied to a case of aortic dissection. In the central and right images it is possible to distinguish the two lumina of a dissected aorta. The presence of two channels introduces further uncertainty in the manual task. The red planes (left and central images) are adjusted so that they are orthogonal to the aorta from two different orientations. The violet and green planes are parallel to the blood flow direction. For the specific location, the orthogonal cross section is described by the red plane (rightmost figure).

2.1. Pathology

The aorta is the main artery in the human body. Microscopically, the aortic wall consists of three layers: a thin intima, a thick and elastic media, an outer-most and fibrous adventitia (Sherifova and Holzapfel (2019)). Aortic dissection is characterized by a splitting and delamination of these layers resulting in a new flow channel – the false lumen (FL) – which is separated from the original true lumen (TL) by the delaminated portion of the aortic wall, called the dissection flap (Figure 3) (Sherifova and Holzapfel (2019)). The origin of this delamination is referred to as *entry tear*, which creates the communication between TL and FL, and *may* be followed by one or more *re-entry tears*, which allow blood to flow back to the TL. AD weakens the aortic wall and may cause a range of life-threatening complications (Slonim et al. (1996)).

2.2. Clinical surveillance

Patients with AD undergo CTA imaging for their initial diagnosis, and for the rest of their lives after hospital discharge, typically after 3 months, 6 months, 12 months, and annually thereafter. Surveillance imaging includes orthogonal diameter measurements along the aorta at specific landmark positions (Müller-Eschner et al. (2013); Mistelbauer et al. (2016); Díaz-Peláez et al. (2017); Nienaber et al. (2016); Bhave et al. (2018); Cao et al. (2019); Hahn et al. (2020); Houben et al. (2020)). A diameter larger than 55 mm is usually an indicator for eligible surgery (Heuts et al. (2020)). This threshold was determined based on the risk of aortic rupture (Nienaber et al. (2016)). Examples of additional indicators are quality of arterial perfusion and overall extension of the FL, to exclude the imminent risk of ischemic complications (Slonim et al. (1996)).

After CTA acquisition, aortic diameters are measured in orthogonal views obtained through a reformation process (Kauffmann et al. (2011); Nienaber et al. (2016); Díaz-Peláez et al. (2017)). Examples of reformation techniques are the manual, double-oblique reformation (Kauffmann et al. (2011)) and the curved multi-planar reformation (Kanitsar et al. (2002); Hahn et al. (2020)). The double-oblique reformation consists in visually determining a new coordinate system for which the XY plane appears orthogonal to the specific location of the aorta, while the planes YZ and XZ are parallel to aortic wall direction in the sagittal and coronal views, respectively (Figure 5) (Kauffmann et al. (2011)). To automate this process, curved multi-planar reformations were introduced (Kanitsar et al. (2002); Hahn et al. (2020)). In this case, the cross-sectional views are considered as orthogonal to the centerline of the aorta. It is important to distinguish the centerline of the overall aorta, used for clinical surveillance (Hahn et al. (2020)), from the centerline of the TL, which is used for surgical planning (Zhao and Feng (2021)). A comparative example is shown in Figure 2. In this work, we focus on applications for clinical surveillance.

2.3. AD image analysis

Technically, the previously mentioned centerlines can be obtained by applying tracking filters (Krissian et al. (2014)) or through thinning of the segmentation, i.e., skeletonization (Hahn et al. (2020)). However, clinical validation showed that diameter measurements obtained through multi-planar reformations tend to fail or overestimate the aortic diameter in patients with aortic dissection or aneurysm, especially in presence of an aortic thrombus, where tracking methods fail (Kauffmann et al. (2011); Krissian et al. (2014)), or, track the two lumina separately (Krissian et al. (2014)). Only recently, CNN-based segmentation approaches showed higher robustness also in presence of thrombus (Cao et al. (2019); Hahn et al. (2020); Cheng et al. (2020); Chen et al. (2021)).

These recent methods provided similar accuracy, although Chen et al. (2021) were also able to simultaneously segment the major arteries. For our purposes, the evaluation of Hahn et al. (2020) is of special interest. The authors specifically evaluated their method on cross-sectional view selection. Their CNN was trained and evaluated on 153 manually labelled CTA volumes and can be used to segment the two lumina of a dissected aorta in presence of thrombus. They used the segmentation of the two

lumina to compute the centerline of the overall aorta and retrieve the cross-sectional planes. Although this approach delivers a valid solution, the accurate manual labelling of a conspicuous number of volumes is often not viable in small and medium-sized clinics. An experienced radiologist requires one to two hours to manually label one dissected aorta, therefore, *preparing 150 cases requires two months of full-time work, excluding review and revision*. Public collections with labelled volumes can often be a solution to support research and clinical centers, but these are difficult to obtain for each different aortic pathology, and the quality of the imaging data could differ from clinic to clinic (Pepe et al. (2020)). We expect this effort to be comparable to that of the other studies, although a complete description is not available.

2.4. Uncertainty-aware deep learning

Deep learning showed impressive results over the last years, also in medical image analysis (Shen et al. (2017)). However, its clinical application is limited by its lack of robustness. Recent reviews and editorials on deep learning are explicitly pointing out to the importance of task reproducibility in medicine (Park (2019); Stupple et al. (2019); Haibe Kains et al. (2020)). It has also been pointed out how the high accuracy of a (deep learning) model does not guarantee the validity of the model for real-world applications (Li et al. (2020)). Therefore, it is essential to define supervision strategies that can help a user monitor patient-level predictions and possibly correct them, especially when reliability and reproducibility are key factors (Begoli et al. (2019); Jungo and Reyes (2019)). An important factor for model validation is the robustness against different, and likely imperfect, references and, therefore, against a non-negligible data uncertainty (e.g., quality of the input). This translates in expecting not only a high accuracy, but also a low model uncertainty. Additionally, this uncertainty can be used to support decision-making processes or to enable fast and effective corrections of the computed results. Recent works started to investigate this aspect, particularly for image segmentation tasks (Jungo and Reyes (2019); Wang et al. (2019)).

Convolutional neural networks have found a number of applications for predictive tasks in biomedical imaging (Xie et al. (2015)). Yet, their coupling with data and model uncertainty has been less intensively investigated. Kendall and Gall (2017) evaluated the impact of data and model uncertainty in computer vision applications using Bayesian neural networks. They showed how model (or epistemic) uncertainty becomes less relevant compared to data uncertainty when the model is trained on large data collections. Vice versa, model uncertainty becomes critical when the model is trained on smaller collections. This is relevant in medical image analysis, where it is difficult to collect large amounts of labelled data for rare diseases. Classical neural networks do not quantify model uncertainty, and Bayesian neural networks, which describe the weight parameters as distributions over the parameters $\omega_i = f(\mu_i, \sigma_i)$ (Kendall and Gall (2017)), can be harder to train, especially in 3D medical imaging, where data can be scarce and requires higher computational costs (Gal and Ghahramani (2016); Li et al. (2021)). An alternative approach is to train K models independently. Given the data pairs (\mathbf{x}, \mathbf{y}) , and the weights' distribution \mathcal{D} , the output distribution of the model $p(\mathbf{y}|\mathbf{x}, \mathcal{D})$ can be represented, empirically, as the mean and variance of the K independent predictions. This can be achieved, for example, by training the K models using bootstrapping (Lakshminarayanan et al. (2017)). Alternatively, Gal and Ghahramani

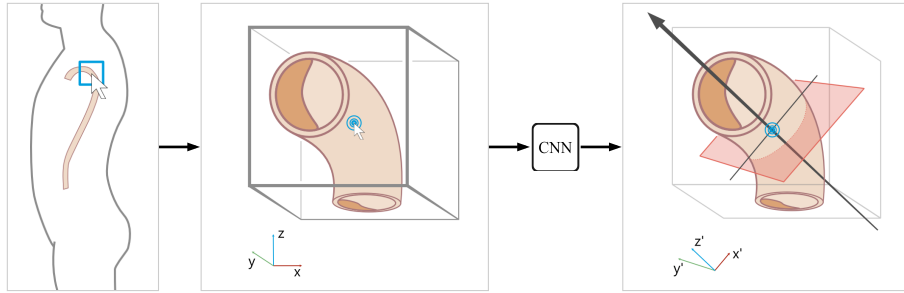


Figure 6: Illustration of the processing pipeline. From left to right: The user selects the location of interest in a 3D volume; the system extracts a 3D patch centered at the specified location; the proposed deep learning architecture predicts the cross-sectional plane. Although we refer to raw CTA data, only the aorta is shown for simplicity. In particular, we illustrate a dissected aorta, where two flow channels are present, separated by a flap. The flap limits the applicability of centerline tracking algorithms.

(2016) proposed Monte Carlo dropout sampling (MCDS). The authors apply dropout, a common regularization technique used during training (Srivastava et al. (2014)), also during testing. The dropout regularization deactivates a random subset of neurons, implicitly generating a pool of models. Some initial applications of MCDS for CNN detection and segmentation have been recently reported (Leibig et al. (2017); Eaton-Rosen et al. (2018); Ayhan et al. (2020); Nair et al. (2020)). These studies provided promising results, but some effects of dropout uncertainty quantification for a CNN need to be further investigated: The sparse and random deactivation of a neuron brings lower benefits with convolutional layers due to the spatial relation built by the convolutional kernels (Ghiasi et al. (2018)). For a broader overview on deep learning and uncertainty quantification in medical imaging, we refer the reader to recent reviews and contributions from Abdar et al. (2021), Ghesu et al. (2021), and Ghoshal et al. (2021). Following these considerations, we investigate how these methods can be coupled with clinical annotations in the remainder of this work.

3. Method

In this section, we formulate our research hypothesis and expand it into an uncertainty-aware CNN approach for the extraction of the cross-sectional planes.

3.1. Research hypothesis

In the previous section, we discussed the cost of image annotation for AD. An alternative source of data might come from clinical annotations. The routinely performed manual selections of double-oblique reformations in aortic surveillance produces an increasing amount of annotated CTA volumes without additional costs, given the high diffusion of cardiovascular diseases and the need for follow-up examinations at regular time intervals (Mistelbauer et al. (2016)). This sets the ground for the definition and evaluation of specific data-driven approaches, which can leverage the availability of such an amount of data. This can result in less expensive solutions, which need, however, to take into account some important factors: The aortic locations at which

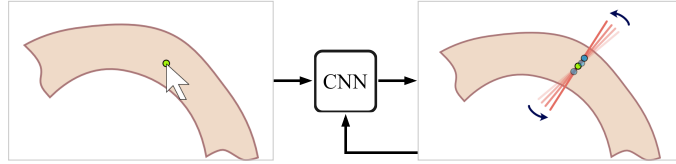


Figure 7: Illustration of the iterative neighbor sampling technique. The user provides an initial pivot point (seed); an iterative process evaluates the robustness of the result by analyzing the plane prediction of neighbor voxels, which lie on the predicted plane.

the measurements are taken may vary from clinic to clinic and from patient to patient; both the plane selection and the measurements are operator-dependent; some less common diseases might be under-represented and more strongly affected by interoperator variations. Moreover, depending on the disease, the sampled data may be scarce or incomplete, and it may show a non-negligible interoperator variability, suggesting the application of uncertainty-aware machine learning models (Begoli et al. (2019)).

3.2. Model architecture

In recent years, convolutional neural networks were applied for regression tasks (Xie et al. (2015)). A typical architecture for regression uses convolutional encoding layers to extract meaningful latent features and fully connected layers to map these features to the desired outputs. A limitation of such an architecture is its inability to represent model uncertainty. Recent studies added dropout layers to the convolutional layers to perform uncertainty quantification through MCDS (Leibig et al. (2017); Nair et al. (2020)). However, current applications of MCDS use dropout regularization with all layers, although this was initially only conceived for fully connected layers (Nair et al. (2020); Ghiasi et al. (2018)). We illustrate our CNN architecture in Figure 8: In the encoding layers (first nine blocks from the left), we use batch normalization and DropBlock (Ghiasi et al. (2018)) to regularize the CNN, max pooling and convolution stride to reduce the number of relevant features. Unlike recent works (Leibig et al. (2017); Nair et al. (2020)), we chose to replace the dropout layers with DropBlock regularization in the encoding layers. This allows us to obtain a Bayesian approximation through Monte Carlo sampling and perform an efficient regularization at the same time. The random deactivation of whole neighborhoods has been shown to provide better regularization in CNN (Ghiasi et al. (2018)). The encoding layers are followed by fully connected layers, which perform the regression from the encoded latent space to the spherical coordinates (θ, ϕ) of the normal vector. Dropout is still applied as a regularization technique on the fully connected layers. As input, for each pivot point P_i , we extract its surrounding patch of size $64 \times 64 \times 64$.

3.3. Training strategy

To prevent overfitting, we augment the training set with random translations. The translation is achieved by considering additional pivot points, which lie on the annotated cross-sectional plane Π_i . These points are collected from a uniform 2D distribution centered in P_i with a radius of $r = 1.53$ mm, which is the standard deviation for

95% LOA of up to ± 3.0 mm. This guarantees higher robustness to inaccuracies during the placement of the pivot points (see [Figure 10](#)). We rely on a 2D distribution as this guarantees that the plane orientations are still correct – orthogonal displacements might require to remeasure the cross-sectional orientations, especially in the ascending aorta or in patients with higher tortuosity. For the training of the network, we employ a batch size of $b = 64$, a learning rate of $l_r = 0.002$, Adam optimizer ([Kingma and Ba \(2015\)](#)), and early stopping. Additionally, due to the periodic nature of the data at hand, we define and apply a circular Huber loss. The standard Huber loss is a piecewise function:

$$H(x, y) = \begin{cases} \frac{1}{2}(x - y)^2, & |x - y| < \delta \\ \delta|x - y| - \frac{1}{2}\delta^2, & \text{otherwise,} \end{cases} \quad (1)$$

where we set $\delta = 1$, as suggested by [Girshick \(2015\)](#).

Although Huber loss has shown to be more robust to outliers than more common losses like \mathcal{L}_1 or \mathcal{L}_2 ([Girshick \(2015\)](#)), it was not meant for periodic functions, such as angles. We defined a circular Huber loss to consider only the acute angles between targets and predictions:

$$H_C(\alpha, \beta) = \begin{cases} H(\alpha, \beta), & |\alpha - \beta| \leq \frac{\pi}{2} \\ H(x, \beta - \text{sign}(\beta) \pi), & \text{otherwise.} \end{cases} \quad (2)$$

It takes into account that the geometrical layout for the reference angles will always be within the closed interval $[-\frac{\pi}{2}, \frac{\pi}{2}]$ and that two angles $\frac{\pi}{2} + k$ and $-\frac{\pi}{2} + k$ describe the same view, i.e., our function is periodic with period π .

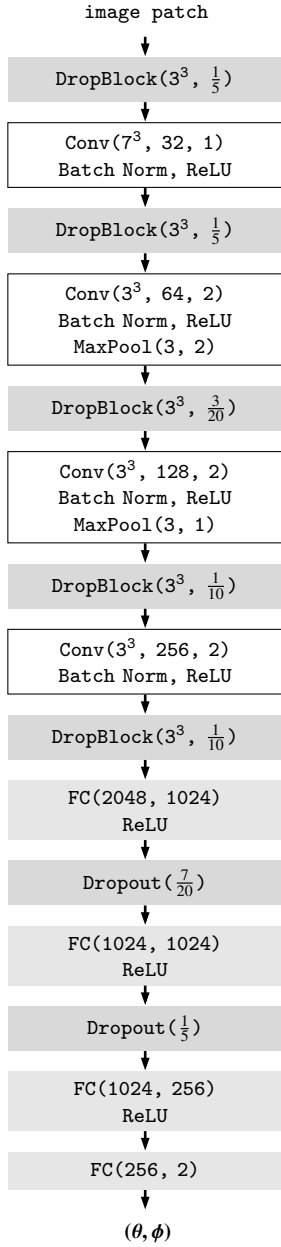


Figure 8: Illustration of the CNN architecture. Legend: DropBlock(K, R) – DropBlock layer with kernel size K and drop rate R; Conv(K, D, S) – convolutional layer with kernel size K, stride S, and D output channels; FC(X, Y) – fully connected layer with X inputs and Y outputs; Dropout(R) – Dropout layer with drop rate R.

3.4. Execution strategy

Interoperator variability of expert annotations is not negligible (Nienaber et al. (2016)). It is therefore important to leverage this information of variability during plane selection. A classic CNN generates a prediction for a given input without providing any information about the uncertainty on the prediction itself. In section 2, we discussed the main approaches for model uncertainty quantification and some of their limitations. Here, we define and evaluate two execution strategies, which extend the concept of MCDS (Gal and Ghahramani (2016)). We refer to these strategies as iterative neighbor sampling (INS) and Monte Carlo DropBlock sampling (MCDBS).

MCDS. Initially suggested by Gal and Ghahramani (2016), MCDS uses the variability produced by the dropout layers to perform a Bayesian approximation through multiple executions. Dropout layers are generally deactivated after the test phase. In MCDS, we do not deactivate these layers, but instead execute the network k times for a given input. The k outputs generate a distribution D_{MC} of possible solutions $(\theta_i, \phi_i)_{i=1, \dots, k}$. We therefore stochastically define our solution as $(\mu_{\theta_i}, \mu_{\phi_i}) \pm (\sigma_{\theta_i}, \sigma_{\phi_i})$, where

$$(\mu_{\theta_i}, \mu_{\phi_i}) = \frac{1}{k} \sum_{n=1}^k \mathcal{M}_n(\mathbf{V}_i, L_i) \quad (3)$$

represents the predictive posterior mean of our measure, and

$$(\sigma_{\theta_i}, \sigma_{\phi_i}) = \frac{1}{k} \sum_{n=1}^k \left[\mathcal{M}_n(\mathbf{V}_i, L_i) - (\mu_{\theta_i}, \mu_{\phi_i}) \right]^2, \quad (4)$$

the uncertainty of our measure. \mathcal{M}_n is the CNN with active dropout at iteration n , \mathbf{V}_i is the input patch, and L_i is the pivot landmark point P_i normalized in $[0, 1]^3$. It is important to note that, for our implementation, MCDS only makes use of dropout layers, and therefore the encoder uncertainty is only partially estimated when considering the uncertainty of the fully connected layers. The reason for this definition will become clearer in the results section.

INS. Instead of observing the variability generated by the dropout layers, at iteration n , we iteratively sample a seed point P_i^n from the plane Π_i^{n-1} predicted at iteration $n-1$ (Figure 7), P_i^1 being the initial pivot point. We sample this point from a uniform distribution, as done for data augmentation, because the network is supposed to be robust to this minimal translation. From each seed point P_i^n , we extract a patch volume \mathbf{V}_i^n , which is centered at this point. We assume that an ideal predictor will generate the same coordinates (θ, ϕ) for any of these points. Again, n iterations will generate a distribution D_{IN} of n possible solutions $(\theta_i, \phi_i)_{i=1, \dots, n}$, if we redefine the predictive posterior mean and the uncertainty $(\mu_{\theta_i}, \mu_{\phi_i}) \pm (\sigma_{\theta_i}, \sigma_{\phi_i})$ as

$$(\mu_{\theta_i}, \mu_{\phi_i}) = \frac{1}{k} \sum_{n=1}^k \mathcal{M}(\mathbf{V}_i^n, L_i^n), \quad (5)$$

and

$$(\sigma_{\theta_i}, \sigma_{\phi_i}) = \frac{1}{k} \sum_{n=1}^k \left[\mathcal{M}(\mathbf{V}_i^n, L_i^n) - (\mu_{\theta_i}, \mu_{\phi_i}) \right]^2. \quad (6)$$

Here the CNN model \mathcal{M} is static and no dropout deactivations are performed. We use this strategy to quantify and reduce the effect of data uncertainty.

MCDbs. Finally, we consider the joint evaluation of encoder and decoder uncertainty. Instead of relying only on the variability introduced by the dropout layers, we leverage the uncertainty provided by the DropBlock layers. We stochastically define our solution $(\sigma_{\theta_i}, \sigma_{\phi_i})$ as in Equation 3 and Equation 4, but here both the encoder and the fully connected layers combined are a random functional \mathcal{M}_n over the execution step n . I.e., both the DropBlock and the Dropout layers are kept active.

4. Results

For the evaluation of our model, we utilize only routinely collected data. All data samples were collected from one single hospital, but randomly processed by 11 different radiology technicians. In this section, we first describe the available data, the pre-processing steps, and evaluate the agreement of the cross-sectional planes extracted by different operators. Afterwards, we report on the accuracy of our model and the improvements introduced by the uncertainty quantification step.

4.1. Data acquisition and reference standard

In total, 162 CTA volumes were acquired from 147 anonymized AD patients undergoing imaging investigation for aortic surveillance purposes. The volumes were of size $512 \times 512 \times Z$ voxels, with $Z = 910 \pm 170$ slices, and an average spacing of $[0.7, 0.7, 0.7]$ mm. Each volume was routinely processed by one out of 11 trained operators between May and December 2020. For each CTA volume, the random operator extracted the relevant cross sections at predefined anatomic locations along the aorta, resulting in 3273 distinct measurements. The anatomical location of predefined aortic landmarks is shown in Figure 9, together with a description of their acronyms. As we deal with clinical annotations, some volumes may present additional measurements or lack some of the defined measurements. Each cross-sectional plane was extracted manually using a double-oblique reformation tool. All manual processing was performed using state-of-the-art commercial medical image processing software (Aquarius iNtuition, TeraRecon, Inc). To provide a quantification of the interoperator variability, 12 CTA volumes were processed three times each, by three different operators. We asked the operators to specifically measure the aortic diameters at all the locations of interest (Figure 9). On average, an experienced operator needed 11 s to locate the landmark and 35–60 s to perform the double-oblique reformation, for each landmark. As a comparison, for healthy aortae, 10 s were sufficient to perform the manual reformation. Furthermore, we also i) segmented these 12 CTA volumes using the trained CNN provided by Hahn et al. (2020) and ii) additionally tracked the centerlines according to Krissian et al. (2014), which allowed us to retrieve the overall aortic centerline for two further methodological references.

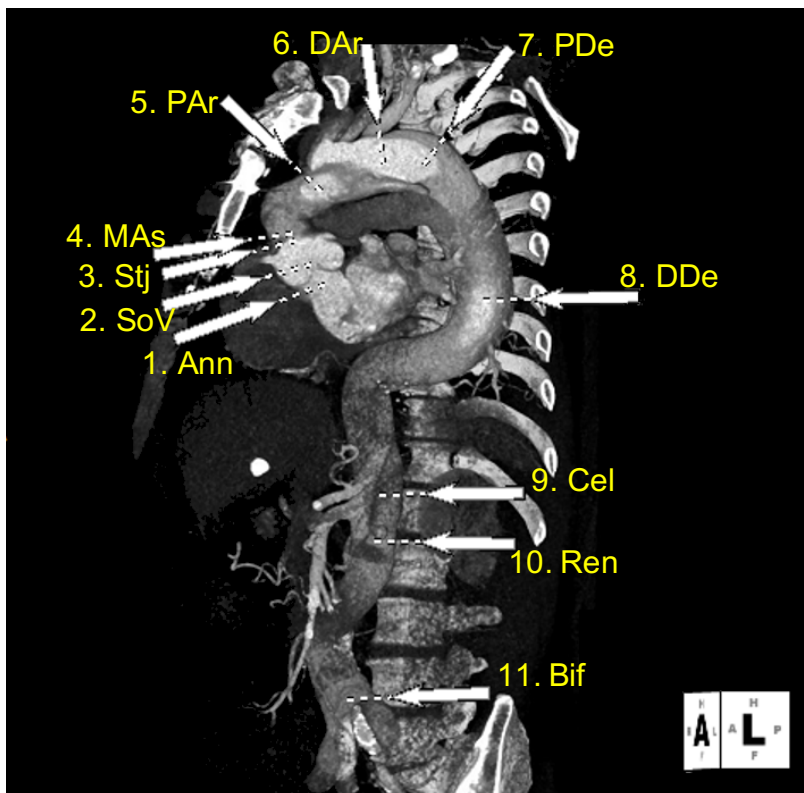


Figure 9: A detailed view of the aortic landmarks at which the measurements were taken. The rendered image shows a case of aortic dissection. The false lumen is clearly distinguishable at the aortic arch. Legend: 1) Aortic annulus (Ann); 2) sinuses of Valsalva (SoV); 3) sinotubular junction (Stj); 4) mid ascending aorta (MAs); 5) proximal aortic arch (PAr); 6) Distal aortic arch (DAr); 7) proximal descending aorta (PDe); 8) distal descending aorta (DDe); 9) aorta at celiac artery (Cel); 10) aorta at inferior main renal artery (Ren); 11) just above iliac bifurcation (Bif). Color image available online.

4.2. Pre-processing

The annotations were initially saved with the proprietary format of Aquarius iNtution. For each measurement location i , we extracted the measurement plane Π_i previously selected by the operator using double-oblique reformation. Each plane Π_i is individually defined by a landmark point $P_i \in \mathbb{R}^3$ and its normal vector $\mathbf{n}_i \in \mathbb{R}^3$. Landmark point P_i was chosen by the operator as the pivot of the measurement plane. For process automation, the estimation of the unit normal vector \mathbf{n}_i would generally require a regression of the three variables (x, y, z) . To reduce complexity, we use spherical coordinates $(r = 1, \theta, \phi)$. This representation simplifies the problem to the estimation of the two variables $(\theta, \phi) \in [0, \pi] \times [-\frac{\pi}{2}, \frac{\pi}{2}]$. For training and testing of our model, we shift θ to the range $[-\frac{\pi}{2}, \frac{\pi}{2}]$ and then normalize the voxel intensity values, as well as θ and ϕ , to the range $[-1, 1]$.

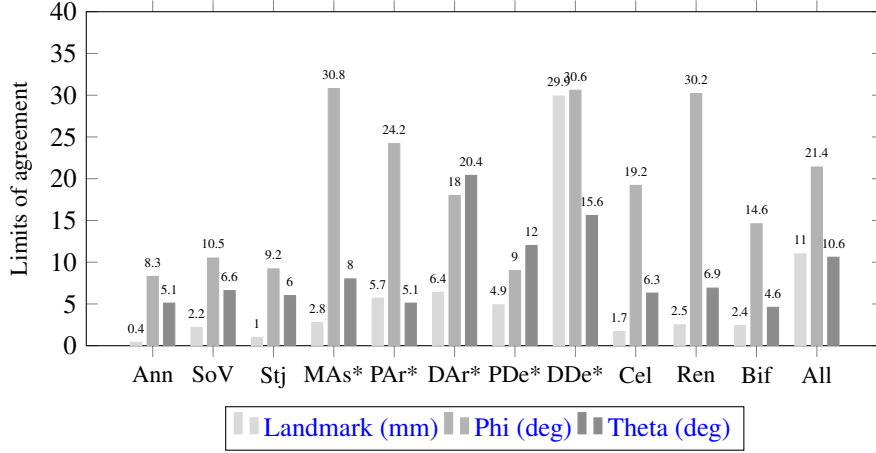


Figure 10: Limits of agreement of the interoperator variability for the placement of the clinical landmarks and the orientations of the cross-sectional views. All limits were calculated according to Jones et al. (2011). We do not show the bias as this is intrinsically zero. *All* refers to the overall variability among all landmarks and operators. *) Higher variabilities for PAR, DAR, PDe and, particularly, DDe were expected due to their rather ill-defined nature. For a description of the acronyms, please refer to Figure 9.

4.3. Data analysis

We analyzed the interoperator variability of *three* operators on the same subset of 12 CTA volumes, which were also segmented. For this purpose, we used the Jones method (Jones et al. (2011)), which defines the variance of m measurements performed by n operators as

$$\sigma^2 = \frac{1}{n-1} \sum_{i=1}^n \left[\frac{1}{m-1} \sum_{j=1}^m (d_{ij} - \bar{d}_i)^2 \right], \quad (7)$$

where d_{ij} is the difference between the j -th measurement of operator i and the mean difference for j , and \bar{d}_i is the mean difference for operator i . The 95% limits of agreement (LOA) with the mean are estimated as $\text{LOA} = \pm 1.96\sigma$. These limits show the uncertainty range which includes 95% of the measurements. We set $n = 3$ as the number of operators. However, it can be shown that the LOA are equivalent to the more common Bland-Altman limits for the case of $n = 2$ operators (Jones et al. (2011)).

We computed the LOA for the landmark positioning, the angles (θ, ϕ), and the major-axis diameters. The overall LOA for the landmark positioning were ± 10.96 mm (Figure 10). In a detailed analysis, we saw that anatomically well-defined landmarks, such as *Ann*, *Stj* and *Cel*, showed LOA between ± 0.44 mm and ± 2.80 mm, while rather ill-defined landmarks, such as *DAR*, *PDe*, and *DDe*, showed LOA of up to ± 6.44 mm, ± 4.88 mm, and ± 29.94 mm, respectively. The actual position of these landmarks is shown in Figure 9. Although clinically relevant, these landmarks are only qualitatively defined as proximal or distal to a reference anatomical structure, which motivates the larger LOA. We chose not to remove these landmarks from our evaluation in order to

Table 1: Comparison of the regularization methods. A) Baseline: Dropout regularization is applied only to the fully connected layers; b) Enc. Dropout: Dropout regularization is applied also to the convolutional layers; c) DropBlock: DropBlock regularization is applied to the convolutional layers and Dropout regularization to the fully connected layers. MAE: Mean absolute error.

CNN Config	Huber	Huber	θ -MAE Valid. set	ϕ -MAE Valid. set
	loss Train set	loss Valid. set	[deg]	[deg]
a) Baseline	0.003	0.019	5.75 ± 1.03	15.74 ± 1.93
b) (a) + Enc. Dropout	0.002	0.020	6.65 ± 0.98	16.01 ± 1.90
c) (a) + DropBlock	0.004	0.019	$6.35 \pm \mathbf{0.70}$	$15.72 \pm \mathbf{1.20}$

see the change in performance in relation to the user’s accuracy. The major-axis diameters showed LOA of ± 5.33 mm, in line with ranges reported in the literature (Nienaber et al. (2016)). The LOA decreased to ± 2.90 mm when DDe was excluded, which shows the general robustness of the manual annotation. For the two angles (θ, ϕ), the LOA are reported in Figure 10 for each landmark and combined. In particular, it can be seen how the determination of ϕ constitutes a less reproducible task than the determination of θ . The overall LOA were $\pm 21.39^\circ$ and $\pm 10.60^\circ$, respectively. We show the impact of this variability on our model in the next sections.

4.4. Regression study

After data collection and analysis, we trained our model on 127 CTA volumes and a total of 2556 measurements. We used the remaining 35 volumes for validation (27) and testing (12). The testing was conducted on the same 12 volumes which were annotated by three experts. Each measurement sample was augmented during training by translating the pivot point (landmark) as previously described. The application was implemented using PyTorch v1.5 and Python v3.7.6. The training was performed on a Linux workstation (GPU: 2× NVidia GeForce RTX 2080Ti, CPU: AMD Threadripper 3960X, 128GB RAM). The training was terminated using an early-stopping approach after 47 epochs for the baseline model, 61 epochs for the dropout approach and 142 epochs for the DropBlock approach. As expected, the regularization affects the duration of the training. Table 1 shows the effect of two different regularization techniques compared to the baseline CNN, where the dropout layers are only placed near the fully connected layers. The regularizations, and particularly DropBlock, appear to reduce the dynamic error related to the predictions. This error is of particular interest in this study, given the focus on reproducibility. For a more comprehensive overview, Table 2 shows the prediction errors on a per-landmark basis as well as the overall error on the test set. All errors are averaged among the ground truths from the three operators. For comparison, we also report the errors obtained with the methods from Hahn et al. (2020) and Krissian et al. (2014). We also need to state that: i) Hahn et al. (2020) can require a manual refinement of the segmentation and ii) Krissian et al. (2014) requires tuning of different hyperparameters, both leading to an increase in operation times.

Table 2: Evaluation of the plain CNN predictions on the 12 test volumes with segmentation and interoperator variability. All errors are averaged among the three operators. For a comparison with the available literature, we also compare the centerline approaches of [Hahn et al. \(2020\)](#) (Hahn) and [Krissian et al. \(2014\)](#) (Krissian) against the three operators. The clinical landmarks marked with * are susceptible to a higher variability due to their ill-posed nature, as shown also in [Figure 10](#).

Landmark	Method	θ -MAE [deg]	ϕ -MAE [deg]
Aortic	NoUQ	4.38	6.94
Annulus (Ann)	Krissian	21.80	26.08
	Hahn	N/A	N/A
Sinuses of Valsalva (SoV)	NoUQ	3.32	9.07
	Krissian	18.09	34.80
	Hahn	11.51	19.68
Sinotubular Junction (Stj)	NoUQ	2.30	11.74
	Krissian	19.41	21.24
	Hahn	9.05	19.46
Mid Ascending A. (MAs)	NoUQ	4.87	15.31
	Krissian	14.96	19.05
	Hahn	12.64	21.72
Proximal Arch (PAr)	NoUQ	6.24	17.86
	Krissian	18.29	18.59
	Hahn	10.38	17.34
Distal Arch (DAr)	NoUQ	12.55	10.23
	Krissian	10.74	7.45
	Hahn	9.36	10.53
Proximal Descending A. (PDe)*	NoUQ	11.67	21.81
	Krissian	10.86	7.74
	Hahn	9.21	6.30
Distal Descending A. (DDe)*	NoUQ	6.62	19.82
	Krissian	9.57	16.22
	Hahn	5.68	9.99
A. at celiac artery (Cel)	NoUQ	3.89	33.95
	Krissian	13.52	34.37
	Hahn	4.99	16.44
A. at inf. main renal art. (Ren)	NoUQ	3.93	26.86
	Krissian	7.07	22.21
	Hahn	4.82	24.30
Above iliac bifur. (Bif)	NoUQ	4.03	9.35
	Krissian*	11.21	23.05
	Hahn	11.19	20.61
Overall (All)	NoUQ	5.80	16.63
	Krissian*	14.21	21.01
	Hahn	8.88	16.64

Table 3: Evaluation of the different execution strategies for uncertainty quantification. Each execution strategy (ES) is evaluated over a different number of iterations k . As a comparison, NoUQ reports the mean absolute errors for $k = 1$, where no uncertainty quantification is performed. The values $\mu \pm \sigma$ correspond to the mean of MAE and standard deviation per measure calculated using the specific execution strategy. Time shows the average execution time for one test sample. For MCDS, only the fully connected layers are re-executed, providing lower execution time than MCDbS.

k	ES	Huber loss	θ -MAE [deg]	ϕ -MAE [deg]	Time [s]
1	NoUQ	0.015	7.48	12.40	0.004
5	INS	0.018 ± 0.003	6.35 ± 1.10	15.52 ± 1.80	0.24
	MCDS	0.016 ± 0.003	6.58 ± 1.30	13.97 ± 2.35	0.01
	MCDbS	0.014 ± 0.004	5.44 ± 1.42	12.02 ± 2.98	0.02
10	INS	0.017 ± 0.003	6.55 ± 0.89	14.75 ± 1.81	0.48
	MCDS	0.016 ± 0.003	6.56 ± 1.43	14.56 ± 2.57	0.01
	MCDbS	0.015 ± 0.005	5.43 ± 1.64	12.29 ± 3.22	0.04
40	INS	0.017 ± 0.003	6.54 ± 0.92	14.84 ± 1.78	1.90
	MCDS	0.016 ± 0.004	6.57 ± 1.52	14.03 ± 2.89	0.04
	MCDbS	0.015 ± 0.005	5.45 ± 1.74	12.28 ± 3.58	0.12
90	INS	0.015 ± 0.001	7.49 ± 0.32	12.62 ± 0.67	4.09
	MCDS	0.016 ± 0.004	6.58 ± 1.52	14.09 ± 2.87	0.08
	MCDbS	0.014 ± 0.005	5.42 ± 1.76	12.12 ± 3.66	0.26

In both cases, the process took between 10 and 25 minutes per volume, excluding landmark selection. Additionally, to compare the reproducibility of the plane selection obtained with three approaches (manual, centerline, and CNN), we measured the 95% limits of agreement with the mean (Jones et al. (2011)). The limits are shown in Figure 11 for each landmark and overall. For the centerline (Hahn et al. (2020)) and CNN (ours) approaches, we used the same landmark positions, which were previously chosen for the manual double-oblique approach – this to avoid any bias due to temporal task repetition or a different user interface than the clinically approved software. It can be seen how both the centerline method and the CNN method provide a higher reproducibility of the plane selection, with the CNN approach providing lower overall limits of agreement of $\approx -27\%$ per angle compared to Hahn et al. (2020) and $\approx -52\%$ compared to the manual annotations.

4.5. Evaluation of uncertainty

In Table 3, we report a comparison of the three execution approaches for different numbers of executions k over all the 35 volumes. In particular, the table shows the average time needed to compute the uncertainty for one sample. The first line, $k = 1$, reports the average error and execution time without uncertainty quantification (NoUQ). Table 4 shows a detailed comparison of the execution approaches for each landmark. The errors are averaged over the annotations of the three operators. ?? shows the overall effect of iterative sampling for all landmarks from the point of view

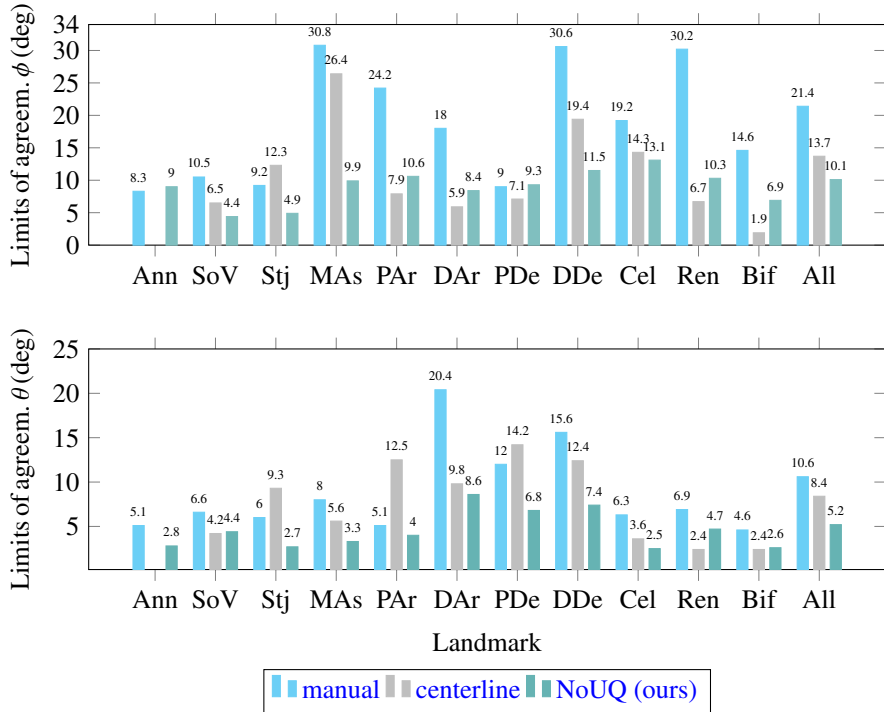


Figure 11: Limits of agreement (95%) of the interoperator variability for the two angles (θ, ϕ) according to Jones et al. (2011) (absolute values, **lower values are better**). For better readability, we do not report biases: these are zero in all cases, given we measure the variability against the mean. *All* refers to the overall variability among landmarks and operators. Lower limits of agreement correspond to a higher reproducibility of the results. For each landmark, *manual* refers to double-oblique reformation, *centerline* to Hahn et al. (2020), and *NoUQ* to our method without uncertainty quantification (UQ). The effect of UQ is reported separately.

of reproducibility. In comparison to Figure 11, iterative sampling provides a considerable improvement on ϕ , which is characterized by a higher interoperator variability in the training data, as previously shown.

5. Discussion

We introduced how surveillance of AD patients requires cross-sectional aortic measurements in CTA imaging. Although centerline analysis is recommended, this remains a challenging and expensive task for AD. Hence, manual double-oblique reformation is usually preferred for patients with challenging aortic conditions, like AD. This generates a growing amount of valid data in the clinical routine, although the interoperator variability between highly trained operators cannot be ignored. Our CNN, trained only on routinely collected data, was able to generalize well even if training and test samples were generated by 11 different operators. Nonetheless, the accuracy of the model alone does not guarantee model validity (Li et al. (2020)). Therefore, we further examined the

Table 4: Evaluation of the different approaches on the 12 test volumes with segmentation and interoperator variability. We provide a comparison of the different execution strategies against the three operators. The clinical landmarks marked with * are susceptible to a higher variability due to their ill-posed nature, as shown also in Figure 10.

Landmark	ES	θ -MAE [deg]	ϕ -MAE [deg]
Aortic	INS	4.38 \pm 0.17	6.92 \pm 0.47
Annulus	MCDS	4.37 \pm 1.37	6.88 \pm 2.34
(Ann)	MCDbS	3.00 \pm 1.24	4.95 \pm 1.87
Sinuses of	INS	3.30 \pm 0.15	9.06 \pm 0.50
Valsalva	MCDS	3.31 \pm 1.29	9.23 \pm 2.42
(SoV)	MCDbS	3.49 \pm 1.28	6.28 \pm 1.61
Sinotubular	INS	2.29 \pm 0.17	11.82 \pm 0.48
Junction	MCDS	2.55 \pm 1.22	11.91 \pm 2.50
(Stj)	MCDbS	3.02 \pm 1.13	4.84 \pm 1.87
Mid	INS	4.87 \pm 0.15	15.52 \pm 0.82
Ascending	MCDS	4.90 \pm 1.29	15.40 \pm 3.07
A. (MAs)	MCDbS	5.47 \pm 1.61	9.13 \pm 2.32
Proximal	INS	6.25 \pm 0.17	17.69 \pm 0.61
Arch	MCDS	6.52 \pm 1.27	17.92 \pm 2.45
(PAr)	MCDbS	4.75 \pm 1.31	9.97 \pm 1.82
Distal	INS	12.54 \pm 0.49	10.30 \pm 0.41
Arch*	MCDS	12.69 \pm 2.04	10.28 \pm 1.89
(DAr)	MCDbS	9.32 \pm 2.09	8.64 \pm 1.88
Proximal	INS	11.66 \pm 0.52	21.71 \pm 0.71
Descending	MCDS	11.91 \pm 2.08	21.81 \pm 3.10
A. (PDe)*	MCDbS	9.53 \pm 2.11	19.44 \pm 2.90
Distal	INS	6.62 \pm 0.30	20.04 \pm 1.14
Descending	MCDS	6.82 \pm 1.83	19.64 \pm 2.98
A. (DDe)*	MCDbS	10.27 \pm 2.33	16.03 \pm 2.95
A. at celiac	INS	3.86 \pm 0.20	34.08 \pm 0.86
artery	MCDS	4.09 \pm 1.63	33.83 \pm 3.98
(Cel)	MCDbS	7.61 \pm 2.17	24.34 \pm 3.77
A. at inf.	INS	3.89 \pm 0.15	26.86 \pm 0.88
main renal	MCDS	4.07 \pm 1.50	26.50 \pm 3.52
art. (Ren)	MCDbS	7.99 \pm 1.93	25.36 \pm 3.90
Above	INS	4.01 \pm 0.13	9.27 \pm 0.60
iliac bifur.	MCDS	4.47 \pm 1.15	9.58 \pm 2.81
(Bif)	MCDbS	4.65 \pm 1.76	7.40 \pm 2.67
Overall	INS	5.81 \pm 0.21	16.62 \pm 0.63
(All)	MCDS	5.99 \pm 1.45	16.90 \pm 2.88
	MCDbS	5.31 \pm 2.77	12.53 \pm 2.65

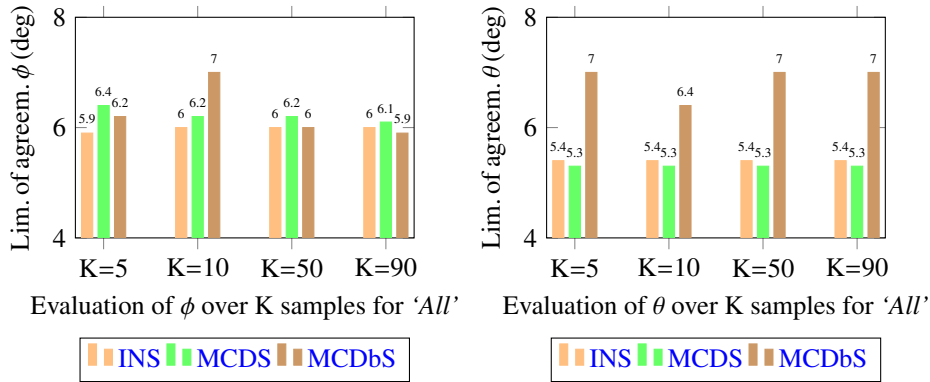


Figure 12: Limits of agreement (95%) of the interoperator variability for the two angles (θ , ϕ) according to Jones et al. (2011) (absolute values, lower values are better). We report the agreement improvement for the overall category after applying the three different uncertainty quantification strategies. Results are to be compared with Figure 11.

robustness of the model against three independent operators and two centerline methods. Although centerline methods are a common standard (Gamechi et al. (2019)), their extraction in AD cases can be expensive or highly inaccurate: CNN segmentation methods are extremely expensive to train (Hahn et al. (2020)) and vessel filters typically generate independent centerlines for the two lumina (Krissian et al. (2014)), which is useful for surgery planning (Zhao and Feng (2021)) but not for surveillance imaging. We posed this as a regression problem, where we predict the direction of the cross-sectional plane. Unlike most machine learning application studies, we did not limit this to an accuracy evaluation, but we further considered the role of uncertainty and validated the model against three independent operators. The remainder of this section provides a more detailed discussion on this matter.

5.1. Effect of regularization and execution strategies

Uncertainty plays a key role when dealing with real-world data. As introduced, a possible approach for model uncertainty quantification is to perform a Monte Carlo sampling of the CNN predictions by leaving the dropout layers active also at test time. However, the introduction of DropBlock as regularization technique for the convolutional layers brought a noticeable reduction of uncertainty, especially for the ϕ angle, characterized by a higher interoperator variability. The evaluation also suggests that the application of dropout solely to the fully connected layers can lead to better performance than applying dropout also to the convolutional layers. Although the resulting MAE is not negligible, the low standard deviation of the network shows a high precision, a relevant factor for task reproducibility. Finally, we observed an interesting relation between the evaluated approaches and the interoperator variability of the training set: for variables with a relatively lower variability, like θ , INS provides often more reliable solutions, characterized by a deviation $\sigma \leq 0.20$ with 10 samples. Variables with higher variability are characterized by an INS deviation above this threshold. In

this case, MCDbS provides a considerably lower error, unless $\sigma \geq 2.50$, where the previous centerline method is still more reliable. These thresholds show where the CNN lacks sufficient training examples to correctly generalize on test data. *Thanks to the short computation time, both methods can be executed in parallel, and a simple binary threshold can be used to recommend a solution to the user.*

5.2. CNN performance and time reduction

In [Table 3](#), we observe that the average execution time of the neural network is only 4 ms for single executions without uncertainty quantification (NoUQ). This is in contrast with timings of up to 60 s for the manual reformation and 30 m for the evaluated centerline methods. The relatively short execution time of the CNN makes the approach easily applicable in soft real-time applications, such as the interactive delineation of cross-sectional planes. As expected, the INS approach shows higher computation times, because the updated volume patch V_i^n has to be loaded on the GPU at each execution step n . Nonetheless, $k = 10$ steps appear to be sufficient to quantify the data uncertainty for an overall execution time of 0.48 s. The performance increment with a higher k becomes less relevant compared to execution time. For the specific task, data uncertainty appears to play a less important role than model uncertainty (MCDS and MCDbS). This is in line with the statements from [Kendall and Gall \(2017\)](#), for whom the type of relevant uncertainty depends on the amount of training volumes. Large collections are difficult to find for rare conditions such as AD. MCDS, where only the uncertainty of the fully connected layer is exploited, shows a low computational cost. This is due to the fact that the output of the encoding layer can be static after the first execution, and only the fully connected layers need to be iteratively re-executed. Compared to INS, MCDS slightly reduces the bias at the cost of higher uncertainty. Finally, MCDbS introduces an interesting outcome. For θ , where the interoperator variability is lower ([Figure 11](#)), the biases are lower than the other two methods, at the cost of higher uncertainty. For the angle ϕ , which showed a much higher interoperator variability, the bias reduction is even stronger. This behaviour is more evident in [Table 4](#). In our empirical tests, hybrid approaches between INS and Monte Carlo sampling did not show any improvement on top of the discussed methods. All the approaches are shown in detail in [Table 4](#) and compared to a centerline-base method.

Overall, the CNN approach without uncertainty quantification (NoUQ) shows similar performance to that of the centerline method. A lower error is particularly seen for the angle θ . For this angle, the uncertainty quantification (UQ) strategies introduce small benefits, compared to ϕ . The second angle benefits considerably from the application of MCDbS, which lowers the bias without increasing the uncertainty when compared to MCDS. Observing the landmarks, MCDbS is beneficial in all the cases for ϕ , although it can be noticed that its effects are less strong on ill-posed landmarks (marked with *). Altogether, this suggests that MCDbS is an efficient UQ strategy when the training data is limited and has a high interoperator variability. For larger collections or, in case of θ , when the interoperator variability is low, INS or the state-of-the-art MCDS approach have higher benefits.

Furthermore, this approach did not only reduce the disagreement but also the processing time. For healthy patients, a radiology technologist required up to 30 s to extract one cross-section, while, for AD patients this process required up to 60 s. This

shows how the disease complicates the measurement process. As a comparison, the extraction of smooth centerlines required between 11 min and 23 min per patient, while the suggested approaches require between 4 ms and 0.48 s to perform the same task with an estimation of the uncertainty.

5.3. Task reproducibility

A strong motivation for this work is reproducibility. In [Figure 11](#), we depict the 95% limits of agreement for both angles at each landmark position. It can be seen how the agreement between the three observers is higher when the operator only depicts the landmark point and the plane is retrieved either from the vessel centerline or with the CNN. A remark must be made for the aortic annulus (*Ann*): For this landmark, our method cannot be compared to the centerline method of [Hahn et al. \(2020\)](#): The aortic segmentation does not always correctly include the aortic root, and, due to the thinning process, the centerlines do not cover the extremities of the aorta. We therefore marked the value as not available (N/A) for the centerline method. In general, planes retrieved with the CNN method show higher agreement than those retrieved from centerlines, without requiring segmentation and skeletonization, but relying only on the task learned from cheaper, clinical annotations. Additionally, for excentric diseased cases, such as dissections and aneurysms, the processed centerlines usually do not match the ideal path, and manual smoothing steps are necessary to enhance the quality of the centerline ([Egger et al. \(2012\)](#)). These steps add a further degree of uncertainty to the final result, which cannot be easily quantified. Our method, instead, provides more accurate and reproducible estimations of the planes with their related uncertainty. The uncertainty quantification plays a key role especially for those variables intrinsically characterized by a higher uncertainty, like ϕ . The uncertainty quantification methods evaluated in this paper considerably reduce this uncertainty between operators. As shown in [Figure 11](#) (3-4), with the introduction of these techniques, both the limits of agreement settle at around 5-6 degree, suggesting that this residual disagreement might be due to the uncertainty in landmark placement.

6. Conclusion

In this work, we addressed the clinical problem of retrieving cross-sectional measurement planes of the aorta in CTA volumes, with a particular emphasis on aortic dissections. For these cases, the extraction of the cross-sectional planes is a challenging, time-consuming and considerably uncertain task, which is still performed manually in the clinical routine.

Our approach is centerline- and segmentation-independent, which is important for diseased vessels, and extracts the cross-section from a single landmark point. In particular, we showed how our CNN model can be used to predict the orientation of a cross-sectional plane with a quantification of the model uncertainty. Additionally, we showed how our method performs in comparison to the interoperator variability of three experienced users and against two existing methods. The model appears to generalize well when compared to the average error of an expert user and shows similar, if not better, performance to one of the centerline methods, which instead requires a segmentation of the vessel. We showed how the suggested approach can reduce the 95% limits

of agreement, thus guaranteeing higher reproducibility. Additionally, we showed how the quantification of the encoder uncertainty can help dealing with training data with intrinsically higher interoperator variability.

Future work includes a large-scale, multi-center evaluation of our approach within the clinical routine. In addition, we plan to extend our approach to a broader set of vascular diseases, like carotid artery stenosis (Lanzino et al. (2009)), and to automate the placement of the seed points with automatic landmark detection approaches (Payer et al. (2019)). Uncertainty visualization methods may also leverage the uncertainty information and guide the radiologists to a range of possible solutions.

Acknowledgments

We acknowledge that this work was approved by the Institutional Review Board of Stanford University, School of Medicine (*IRB n. 47939*) and received fundings from the TU Graz LEAD Project *Mechanics, Modeling and Simulation of Aortic Dissection*, the Austrian Science Fund (FWF) *KLI 678-B31 enFaced*, the REACT-EU project KITE (Plattform für KI-Translation Essen), and the Austrian Marshall Plan Foundation Scholarship. Furthermore, we thank all members of the 3D and Quantitative Imaging Laboratory (Stanford University), Lewis D. Hahn (UC San Diego), and Sascha Ranftl (TU Graz).

References

- Abdar, M., Pourpanah, F., Hussain, S., Rezazadegan, D., Liu, L., Ghavamzadeh, M., Fieguth, P., Cao, X., Khosravi, A., Acharya, U.R., et al., 2021. A review of uncertainty quantification in deep learning: Techniques, applications and challenges. *Information Fusion* 76, 243–297. doi:[10.1016/j.inffus.2021.05.008](https://doi.org/10.1016/j.inffus.2021.05.008).
- Ayhan, M.S., Kühlewein, L., Aliyeva, G., Inhoffen, W., Ziemssen, F., Berens, P., 2020. Expert-validated estimation of diagnostic uncertainty for deep neural networks in diabetic retinopathy detection. *Medical Image Analysis* 64, 1–13. doi:[10.1016/j.media.2020.101724](https://doi.org/10.1016/j.media.2020.101724).
- Begoli, E., Bhattacharya, T., Kusnezov, D., 2019. The need for uncertainty quantification in machine-assisted medical decision making. *Nature Machine Intelligence* 1, 20–23. doi:[10.1038/s42256-018-0004-1](https://doi.org/10.1038/s42256-018-0004-1).
- Bhave, N.M., Nienaber, C.A., Clough, R.E., Eagle, K.A., 2018. Multimodality imaging of thoracic aortic diseases in adults. *JACC: Cardiovascular Imaging* 11, 902–919. doi:[10.1016/j.jcmg.2018.03.009](https://doi.org/10.1016/j.jcmg.2018.03.009).
- Cao, L., et al., 2019. Fully automatic segmentation of type b aortic dissection from cta images enabled by deep learning. *European Journal of Radiology* 121, 108713. doi:[10.1016/j.ejrad.2019.108713](https://doi.org/10.1016/j.ejrad.2019.108713).

- Chen, D., Zhang, X., Mei, Y., Liao, F., Xu, H., Li, Z., Xiao, Q., Guo, W., Zhang, H., Yan, T., et al., 2021. Multi-stage learning for segmentation of aortic dissections using a prior aortic anatomy simplification. *Medical Image Analysis* 69, 101931. doi:[10.1016/j.media.2020.101931](https://doi.org/10.1016/j.media.2020.101931).
- Cheng, J., Tian, S., Yu, L., Ma, X., Xing, Y., 2020. A deep learning algorithm using contrast-enhanced computed tomography (CT) images for segmentation and rapid automatic detection of aortic dissection. *Biomedical Signal Processing and Control* 62, 102145. doi:[10.1016/j.bspc.2020.102145](https://doi.org/10.1016/j.bspc.2020.102145).
- Díaz-Peláez, E., Barreiro-Pérez, M., Martín-García, A., Sanchez, P.L., 2017. Measuring the aorta in the era of multimodality imaging: still to be agreed. *Journal of Thoracic Disease* 9, S445–447. doi:[10.21037/jtd.2017.03.96](https://doi.org/10.21037/jtd.2017.03.96).
- Eaton-Rosen, Z., Bragman, F., Bisdas, S., Ourselin, S., Cardoso, M.J., 2018. Towards safe deep learning: Accurately quantifying biomarker uncertainty in neural network predictions, in: *International Conference on Medical Image Computing and Computer-Assisted Intervention*, pp. 691–669. doi:[10.1007/978-3-030-00928-1_78](https://doi.org/10.1007/978-3-030-00928-1_78).
- Egger, J., Grosskopf, S., Nimsky, C., Kapur, T., Freisleben, B., 2012. Modeling and visualization techniques for virtual stenting of aneurysms and stenoses. *Computerized Medical Imaging and Graphics* 36, 183–203. doi:[10.1016/j.compmedimag.2011.12.002](https://doi.org/10.1016/j.compmedimag.2011.12.002).
- Erbel, R., et al., 2014. 2014 ESC guidelines on the diagnosis and treatment of aortic diseases. *European Heart Journal* 35, 2873–2926. doi:[10.1093/eurheartj/ehu281](https://doi.org/10.1093/eurheartj/ehu281).
- Gal, Y., Ghahramani, Z., 2016. Dropout as a bayesian approximation: Representing model uncertainty in deep learning, in: *International Conference on Machine Learning*, pp. 1050–1059. URL: <https://dl.acm.org/doi/10.5555/3045390.3045502>.
- Gamechi, Z.S., Bons, L.R., Giordano, M., Bos, D., Budde, R.P.J., Kofoed, K.F., Pedersen, J.H., Roos-Hesselink, J.W., de Bruijne, M., 2019. Automated 3D segmentation and diameter measurement of the thoracic aorta on non-contrast enhanced CT. *European Radiology* 29, 4613–4623. doi:[10.1007/s00330-018-5931-z](https://doi.org/10.1007/s00330-018-5931-z).
- Ghesu, F.C., Georgescu, B., Mansoor, A., Yoo, Y., Gibson, E., Vishwanath, R., Balachandran, A., Balter, J.M., Cao, Y., Singh, R., et al., 2021. Quantifying and leveraging predictive uncertainty for medical image assessment. *Medical Image Analysis* 68, 101855. doi:[10.1016/j.media.2020.101855](https://doi.org/10.1016/j.media.2020.101855).
- Ghiasi, G., Lin, T.Y., Le, Q.V., 2018. Dropblock: A regularization method for convolutional networks, in: *Conference on Neural Information Processing Systems*, pp. 10750–10760. URL: <https://dl.acm.org/doi/10.5555/3327546.3327732>.
- Ghoshal, B., Tucker, A., Sanghera, B., Lup Wong, W., 2021. Estimating uncertainty in deep learning for reporting confidence to clinicians in medical image segmentation

- and diseases detection. *Computational Intelligence* 37, 701–734. doi:[10.1111/coin.12411](https://doi.org/10.1111/coin.12411).
- Girshick, R., 2015. Fast r-cnn, in: *International Conference on Computer Vision*, pp. 1440–1448. doi:[10.1109/ICCV.2015.169](https://doi.org/10.1109/ICCV.2015.169).
- Hahn, L.D., et al., 2020. Ct-based true- and false-lumen segmentation in type B aortic dissection using machine learning. *Radiology: Cardiothoracic Imaging* 2, 1–10. doi:[10.1148/ryct.2020190179](https://doi.org/10.1148/ryct.2020190179).
- Haibe Kains, B., et al., 2020. Transparency and reproducibility in artificial intelligence. *Nature* 586, E14–E16. doi:[10.1038/s41586-020-2766-y](https://doi.org/10.1038/s41586-020-2766-y).
- Heuts, S., et al., 2020. Evaluating the diagnostic accuracy of maximal aortic diameter, length and volume for prediction of aortic dissection. *Heart* 106, 892–897. doi:[10.1136/heartjnl-2019-316251](https://doi.org/10.1136/heartjnl-2019-316251).
- Houben, I.B., van Bakel, T.M.J., Burris, N.S., Moll, F.L., van Herwaarden, J.A., Patel, H.J., 2020. Critical appraisal of multidimensional CT measurements following acute open repair of type A aortic dissection. *Journal of Cardiac Surgery* , 634–644doi:[10.1111/jocs.14446](https://doi.org/10.1111/jocs.14446).
- Jones, M., Dobson, A., O’Brian, S., 2011. A graphical method for assessing agreement with the mean between multiple observers using continuous measures. *International Journal of Epidemiology* 30, 1308–1313. doi:[10.1093/ije/dyr109](https://doi.org/10.1093/ije/dyr109).
- Jungo, A., Reyes, M., 2019. Assessing reliability and challenges of uncertainty estimations for medical image segmentation, in: *International Conference on Medical Image Computing and Computer-Assisted Intervention*, Springer. pp. 48–56. doi:[10.1007/978-3-030-32245-8_6](https://doi.org/10.1007/978-3-030-32245-8_6).
- Kanitsar, A., et al., 2002. CPR - curved planar reformation, in: *IEEE Visualization*, pp. 37–44. doi:[10.1109/VISUAL.2002.1183754](https://doi.org/10.1109/VISUAL.2002.1183754).
- Kauffmann, C., Tang, A., Dugas, A., Therasse, E., Oliva, V., Soulez, G., 2011. Clinical validation of a software for quantitative follow-up of abdominal aortic aneurysm maximal diameter and growth by CT angiography. *European Journal of Radiology* 77, 502–508. doi:[10.1016/j.ejrad.2009.07.027](https://doi.org/10.1016/j.ejrad.2009.07.027).
- Kaufhold, L., Harloff, A., Schumann, C., Krafft, A.J., Hennig, J., Hennemut, A., 2018. Image-based assessment of uncertainty in quantification of carotid lumen. *Journal of Medical Imaging* 5, 034003. doi:[10.1117/1.JMI.5.3.034003](https://doi.org/10.1117/1.JMI.5.3.034003).
- Kendall, A., Gall, Y., 2017. What uncertainties do we need in bayesian deep learning for computer vision?, in: *Conference on Neural Information Processing Systems*, pp. 5580–5590. URL: <https://dl.acm.org/doi/10.5555/3295222.3295309>.
- Kingma, D.P., Ba, J.L., 2015. Adam: A method for stochastic optimization, in: *International Conference on Learning Representations*, pp. 1–13. doi:[11245/1.505367](https://doi.org/10.1145/1.505367).

- Krissian, K., Carreira, J.M., Esclarin, J., Maynar, M., 2014. Semi-automatic segmentation and detection of aorta dissection wall in MDCT angiography. *Medical Image Analysis* 18, 83–102. doi:[10.1016/j.media.2013.09.004](https://doi.org/10.1016/j.media.2013.09.004).
- Lakshminarayanan, B., Pritzel, A., Blundell, C., 2017. Simple and scalable predictive uncertainty estimation using deep ensembles, in: *Conference on Neural Information Processing Systems*, pp. 1–12. URL: <https://dl.acm.org/doi/10.5555/3295222.3295387>.
- Lanzino, G., Rabinstein, A.A., Brown, R.D., 2009. Treatment of carotid artery stenosis: Medical therapy, surgery, or stenting? *Mayo Clinic Proceedings* 84, 362–368. doi:[10.1016/S0025-6196\(11\)60546-6](https://doi.org/10.1016/S0025-6196(11)60546-6).
- Lau, C., Feldman, D.N., Girardi, L.N., Kim, L.K., 2017. Epidemiology of thoracic aortic dissection. *Journal of Thoracic Disease* 9, 309–316. doi:[10.21037/jtd.2017.03.89](https://doi.org/10.21037/jtd.2017.03.89).
- Leibig, C., Allken, V., Ayhan, M.S., Berens, P., Wahl, S., 2017. Leveraging uncertainty information from deep neural networks for disease detection. *Nature Scientific Reports* 7, 1–14. doi:[10.1038/s41598-017-17876-z](https://doi.org/10.1038/s41598-017-17876-z).
- Li, J., von Campe, G., Pepe, A., Gsaxner, C., Wang, E., Chen, X., Zefferer, U., Tödting, M., Krall, M., Deutschmann, H., et al., 2021. Automatic skull defect restoration and cranial implant generation for cranioplasty. *Medical Image Analysis* , 102171doi:[10.1016/j.media.2021.102171](https://doi.org/10.1016/j.media.2021.102171).
- Li, J., Liu, L., Le, T.D., Liu, J., 2020. Accurate data-driven prediction does not mean high reproducibility. *Nature Machine Intelligence* 2, 13–15. doi:[10.1038/s42256-019-0140-2](https://doi.org/10.1038/s42256-019-0140-2).
- Lombardi, J.V., Hughes, G.C., Appoo, J.J., Bavaria, J.E., Beck, A.W., Cambria, R.P., Charlton-Ouw, K., Eslami, M.H., Kim, K.M., Leshnower, B.G., Maldonado, T., Reece, T.B., Wang, G.J., 2020. Society for vascular surgery (svs) and society of thoracic surgeons (sts) reporting standards for type b aortic dissections. *Journal of Vascular Surgery* 71, 723–747. doi:[10.1016/j.jvs.2019.11.013](https://doi.org/10.1016/j.jvs.2019.11.013).
- Mistelbauer, G., Schmidt, J., Sailer, A.M., Bäumler, K., Walters, S., Fleischmann, D., 2016. Aortic dissection maps: Comprehensive visualization of aortic dissections for risk assessment, in: *Eurographics Workshop on Visual Computing for Biology and Medicine*, pp. 143–152. doi:[10.2312/vcbm.20161282](https://doi.org/10.2312/vcbm.20161282).
- Müller-Eschner, M., et al., 2013. Accuracy and variability of semiautomatic centerline analysis versus manual aortic measurement techniques for tevar. *European Journal of Vascular and Endovascular Surgery* 45, 241–247. doi:[10.1016/j.ejvs.2012.12.003](https://doi.org/10.1016/j.ejvs.2012.12.003).
- Nair, T., Precup, D., Arnold, D.L., Arbel, T., 2020. Exploring uncertainty measures in deep networks for multiple sclerosis lesion detection and segmentation. *Medical Image Analysis* 59, 1–10. doi:[10.1016/j.media.2019.101557](https://doi.org/10.1016/j.media.2019.101557).

- Nienaber, C.A., Clough, R.E., Sakalihan, N., Suzuki, T., Gibbs, R., Mussa, F., Jenkins, M.P., Thompson, M.M., Evangelista, A., Yeh, J.S.M., Cheshire, N., Rosendahl, U., Pepper, J., 2016. Aortic dissection. *Nature Reviews Disease Primers* 21, 16053. doi:[10.1038/nrdp.2016.53](https://doi.org/10.1038/nrdp.2016.53).
- Park, C.M., 2019. Can artificial intelligence fix the reproducibility problem of radiomics? *Radiology* 292, 374–375. doi:[10.1038/s41586-020-2766-y](https://doi.org/10.1038/s41586-020-2766-y).
- Payer, C., Štern, D., Bischof, H., Urschler, M., 2019. Integrating spatial configuration into heatmap regression based CNNs for landmark localization. *Medical Image Analysis* 54, 207–219. doi:[10.1016/j.media.2019.03.007](https://doi.org/10.1016/j.media.2019.03.007).
- Pepe, A., et al., 2020. Detection, segmentation, simulation and visualization of aortic dissections: A review. *Medical Image Analysis* 64, 1–16. doi:[10.1016/j.media.2020.101773](https://doi.org/10.1016/j.media.2020.101773).
- Rajiah, P., 2013. CT and MRI in the evaluation of thoracic aortic diseases. *International Journal of Vascular Medicine* 2013, 1–16. doi:[10.1155/2013/797189](https://doi.org/10.1155/2013/797189).
- Shen, D., Wu, G., Suk, H.I., 2017. Deep learning in medical image analysis. *Annual Review of Biomedical Engineering* 19, 221–248. doi:[10.1146/annurev-bioeng-071516-044442](https://doi.org/10.1146/annurev-bioeng-071516-044442).
- Sherifova, S., Holzapfel, G.A., 2019. Biomechanics of aortic wall failure with a focus on dissection and aneurysm: a review. *Acta Biomaterialia* 99, 1–17. doi:[10.1016/j.actbio.2019.08.017](https://doi.org/10.1016/j.actbio.2019.08.017).
- Slonim, S.M., Nyman, U., Semba, C.P., Miller, D.C., Mitchell, R.S., Dake, M.D., 1996. Aortic dissection: percutaneous management of ischemic complications with endovascular stents and balloon fenestration. *Journal of vascular surgery* 23, 241–253. doi:[10.1016/s0741-5214\(96\)70268-9](https://doi.org/10.1016/s0741-5214(96)70268-9).
- Srivastava, N., Hinton, G., Krizhevsky, A., Sutskever, I., Salakhutdinov, R., 2014. Dropout: A simple way to prevent neural networks from overfitting. *The Journal of Machine Learning Research* 15, 1929–1958. doi:[10.5555/2627435.2670313](https://doi.org/10.5555/2627435.2670313).
- Stuppel, A., Singerman, D., Celi, L.A., 2019. The reproducibility crisis in the age of digital medicine. *npj Digital Medicine* 2, 1–3. doi:[10.1038/s41746-019-0079-z](https://doi.org/10.1038/s41746-019-0079-z).
- Wang, G., Li, W., Aertsen, M., Deprest, J., Ourselin, S., Vercauteren, T., 2019. Aleatoric uncertainty estimation with test-time augmentation for medical image segmentation with convolutional neural networks. *Neurocomputing* 338, 34–45. doi:[10.1016/j.neucom.2019.01.103](https://doi.org/10.1016/j.neucom.2019.01.103).
- Xie, Y., et al., 2015. Beyond classification: Structured regression for robust cell detection using convolutional neural network, in: *International Conference on Medical Image Computing and Computer-Assisted Intervention*, pp. 358–365. doi:[10.1007/978-3-319-24574-4_43](https://doi.org/10.1007/978-3-319-24574-4_43).
- Zhao, J., Feng, Q., 2021. Automatic aortic dissection centerline extraction via morphology-guided crn tracker. *IEEE Journal of Biomedical and Health Informatics* 25, 3473 – 3485. doi:[10.1109/JBHI.2021.3068420](https://doi.org/10.1109/JBHI.2021.3068420).